nature nanotechnology
SUPPLEMENTARY INFORMATION
DOI: 10.1038/NNANO.2014.31

Graphene photodetectors with ultra-broadband and high responsivity at room temperature

Chang-Hua Liu[1†], You-Chia Chang[2†], Ted Norris[1.2*] and Zhaohui Zhong[1*]

Supplementary Section 1.

Measurement of the capacitance of Ta_2O_5 dielectric layer

To measure the capacitance of Ta_2O_5 dielectric layer, we configure our double layer graphene heterostructure device as a dual gate field-effect transistor (Fig. S2a). Here, the Si substrate is used as the backgate and top graphene layer is served as the top-gate. Sweeping both top-gate voltage (V_{gt}) and the backgate voltage (V_{gb}) can modulate the channel conductance of bottom layer graphene. A 2D colour plot of bottom layer graphene resistance versus both V_{gt} and V_{gb} are shown in Fig. S2b. It is apparent that ambipolar transfer characteristics can be observed with both gate voltage sweeps, with the charge neutrality point ($V_{gb}^{CNP}, V_{gt}^{CNP}$) identified as the local peak in resistance. More importantly, the slope of $\frac{V_{gb}^{CNP}}{V_{gt}^{CNP}} \sim 74$ in the 2D plot gives a direct measurement of the ratio between top-gate capacitance and backgate capacitance[1]. The backgate dielectric is thermal oxide ($\varepsilon_{SiO_2} = 3.9$, Thickness of SiO_2 = 285 nm) with a backgate capacitance of 1.2×10^{-8} F/cm^2. Hence, the gate capacitance of the Ta_2O_5 dielectric layer is calculated to be 8.9×10^{-7} F/cm^2.

© 2014 Macmillan Publishers Limited. All rights reserved.

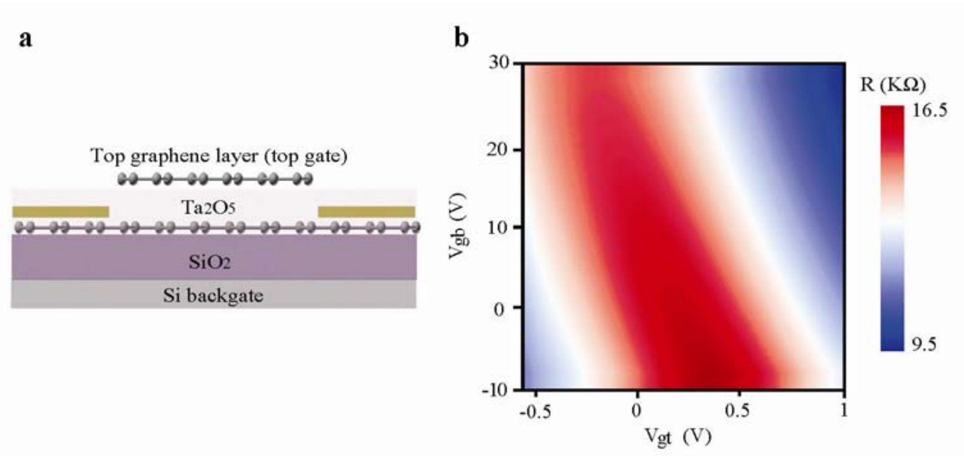

Figure S1 Characterization of the gate capacitance of Ta_2O_5 layer. a, Device structure of a graphene heterostructure photodetector. Here we operate the device as a dual-gate field effect transistor, with silicon substrate as the backgate (V_{gb}), and top graphene layer as the top gate (V_{gt}). (b) Two dimensional plot of the resistance of the bottom graphene layer as a function of V_{gb} and V_{gt}.

Supplementary Section 2.

Measurement of the Fermi energy of two graphene layers

In general, the Fermi energy of graphene can be determined from the ambipolar I-V_g transfer curve[2,3]:

$$E_F = \hbar v_F \sqrt{\pi C \frac{(V_g - V_g^{CNP})}{e}}, \qquad (1)$$

where $\hbar v_F$ = 5.52 eVÅ and C is the gate capacitance for V_g.

In our devices, the Fermi energy of the bottom layer graphene can be readily determined by the backgate voltage (V_{gb}) dependent transfer curve, as shown in Fig S3 (black curves). Using Eq. 1, we can determine the Fermi energies of bottom layer graphene for three representative devices to be 4.652 eV, 4.672 eV, and 4.616 eV, respectively, at V_{gb} = 0 V.

© 2014 Macmillan Publishers Limited. All rights reserved.

For top graphene layer, however, partial screening of the electric field by the bottom layer graphene[1] prevents efficient gating of the Si backgate. In order to determine the Fermi energy of the top layer graphene, we can operate the bottom layer graphene as gate (V_{gm}) and measure its gate effect on the top layer graphene. The gate capacitance can be measured to be 8.9×10^{-7} F/cm^2, using the technique describe in previous section. Hence, the ambipolar V_{gm} dependent transfer curves (Fig S3, red curves) yield the Fermi energies for top layer graphene of the same three devices to be 4.786 eV, 4.769 eV, and 4.775 eV, respectively, at $V_{gm} = 0$ V. All four devices measured (including device shown in Fig. 1b) show higher p-doping for the top layer graphene than the bottom layer graphene. The band bending across the heterostructure can be determined by the Fermi energy difference of two graphene layers to be ~ 0.12 eV.

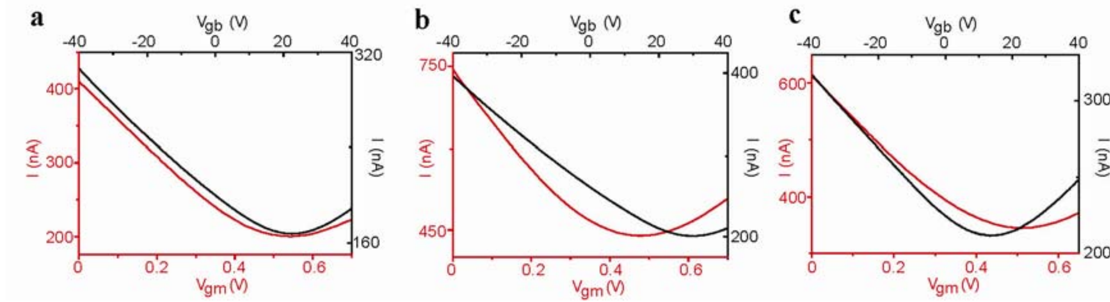

Figure S2 Characterization of the Fermi energy of top and bottom layer graphene. The ambipolar I-V_g transfer curves are shown here for three representative devices, a-c. Transfer curves for bottom layer graphene using Si backgate (V_{gb}) are shown in black. Transfer curves for top layer graphene using bottom layer graphene as gate (V_{gm}) are shown in red. The source-drain bias voltage for all measurements shown is set at 2 mV.

Supplementary Section 3.

Analysis of noise spectral density

© 2014 Macmillan Publishers Limited. All rights reserved.

Noise-equivalent-power (NEP) is an important figure of merit for photodetectors, and it is defined as the optical power that yields a unity signal-to-noise ratio for a given bandwidth. To obtain NEP, we first analyze the noise in the dark current waveform. As shown in Fig. S4a, the dark current waveform was acquired by a current preamplifier and a data acquisition card with a sampling rate of 10 kHz. The source-drain bias voltage applied to the bottom graphene layer was 1V in this measurement. The noise spectral density is given by

$$S(f) = \lim_{T\to\infty} \frac{1}{\sqrt{T}} \sqrt{\left\langle \left| \int_{-T/2}^{T/2} I(t) e^{-i2\pi ft} dt \right|^2 \right\rangle}, \qquad (2)$$

where $\langle \ \rangle$ denotes the expectation value, and $I(t)$ is the current waveform. The definition can be generalized to discrete finite sampling of the current $I(t_n)$:

$$S(f_n) = \frac{1}{\sqrt{F_s N}} \sqrt{\left\langle \left| \boldsymbol{I}(f_n) \right|^2 \right\rangle}, \qquad (3)$$

where $\boldsymbol{I}(f_n)$ denotes the discrete Fourier transform of $I(t_n)$; F_s is the sampling rate; N is the number of data points. Notice that the Fourier transform used here is defined so that $S(f_n)$ is non-zero only at positive frequencies. The unit of $S(f_n)$ is $A/Hz^{1/2}$. Fig. S4b shows the noise spectral density of the dark current calculated by Eq. 3.

In addition, we also measured directly the noise spectral density of the dark current by using a FFT spectrum analyzer (Stanford Research Systems SR760). The measured noise spectral density is shown in Fig. S4c. The results obtained by these two approaches are consistent with each other. NEP can be calculated by dividing the noise spectral density by the responsivity. With visible excitation, the responsivity of graphene photodetector can achieve ~1000 A/W (Fig. 2d), which corresponds to a NEP of ~ 10^{-11} $W/Hz^{1/2}$ at a modulation

© 2014 Macmillan Publishers Limited. All rights reserved.

frequency of 1 Hz.

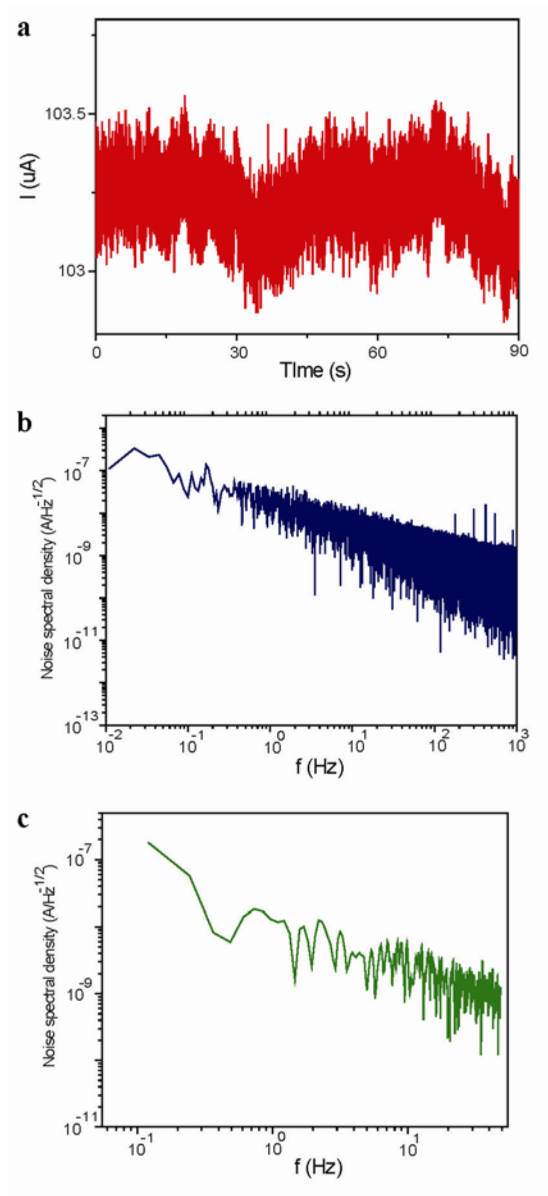

Figure S3 Analysis of noise spectral density of the heterostructure graphene photodetector. **a,** The dark current waveform of the graphene photodetector with source-drain voltage V_{sd} = 1 V. **b**, Analysis of noise spectral density of the graphene photodetector based on the dark current waveform measured in (**a**). **c**, Noise spectral density of the graphene photodetector measured directly by using a commercial FFT spectrum analyzer.

© 2014 Macmillan Publishers Limited. All rights reserved.

Supplementary Section 4.

Scanning photocurrent mapping of individual graphene transistors

We performed spatial mapping of the photocurrent generation within each individual graphene layer by using the scanning photocurrent spectroscopy[4-6]. The schematic of the device and experimental setup is shown in Fig. S1a. The laser spot was focused to 1.5 μm diameter and was raster scanned across the entire device while the current through the graphene transistors within each individual layer was recorded. The laser beam was chopped by mechanical chopper at 1.1 KHz, and the generated short circuit photocurrent was then detected by lock-in amplifier at room temperature in vacuum.

Fig. S1 b and c show the measured scanning photocurrent images from the bottom and top graphene transistors, respectively. Here, the laser excitation wavelength is at 900 nm and excitation power is 600 μW. Both results show two photocurrent peaks near the metal/graphene contact edges with opposite polarity, suggesting photocurrent generation is due to the built-in electric field at the metal/graphene junction[4-6]. We note that these features are different from the photocurrent images in Fig. 3a and 3b of the main text, where hot carrier tunnelling current is generated at the overlapped region of two graphene layers.

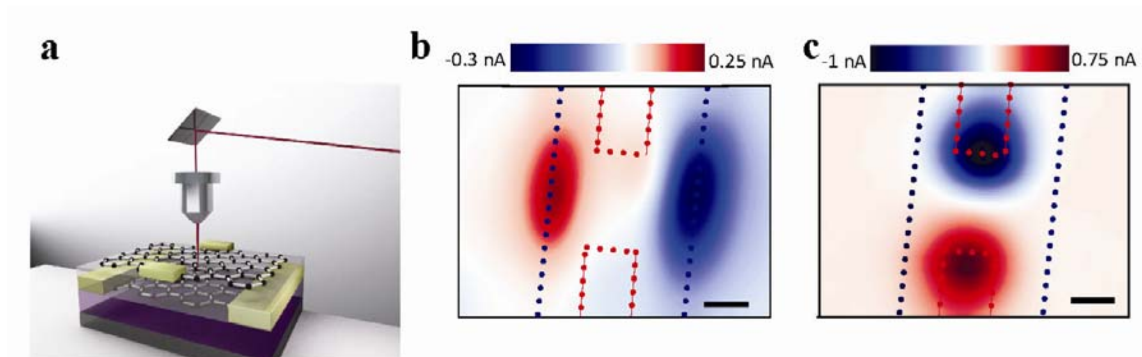

© 2014 Macmillan Publishers Limited. All rights reserved.

Figure S4 Scanning photocurrent measurements of top and bottom layer graphene transistors. a, Schematic drawing of the device and scanning photocurrent measurement setup. **b,** A scanning photocurrent image of the bottom graphene transistor. **c,** A scanning photocurrent image of the top graphene transistor. In both panels b and c, the blue dotted lines indicate the metal/graphene contact edges of bottom graphene transistor, and the red dotted lines indicate the metal/graphene contact edges of top graphene transistor. Scale bars represent 2 μm.

Supplementary Section 5.

Graphene/Ta_2O_5/graphene heterostructure photodetector under near-infrared light illumination

© 2014 Macmillan Publishers Limited. All rights reserved.

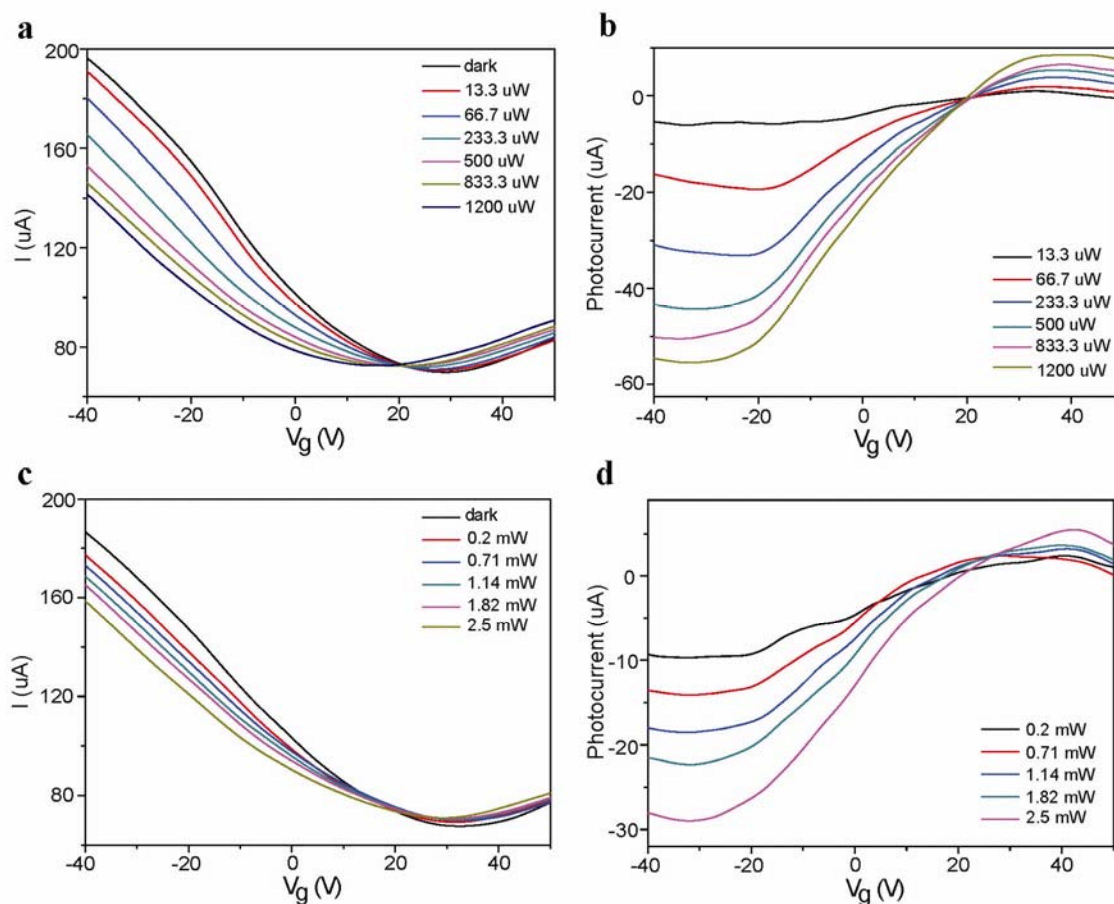

Figure S5 Near-infrared photoresponse of the graphene/Ta_2O_5/graphene heterostructure photodetector. a, I-V_g characteristics of the measured graphene photodetector under different illumination power with the excitation wavelength at 800 nm. V_{SD} = 1V. **b,** Extracted gate dependence of photocurrent (I_{light}- I_{dark}) from results in (a). **c,** I-V_g characteristics of the measured graphene photodetector under different illumination power with the excitation wavelength at 900 nm. V_{SD} = 1V. **d,** Extracted gate dependence of photocurrent (I_{light}- I_{dark}) from results in (**c**).

Supplementary Section 6.

Graphene/Si/graphene heterostructures under mid-infrared light illumination

© 2014 Macmillan Publishers Limited. All rights reserved.

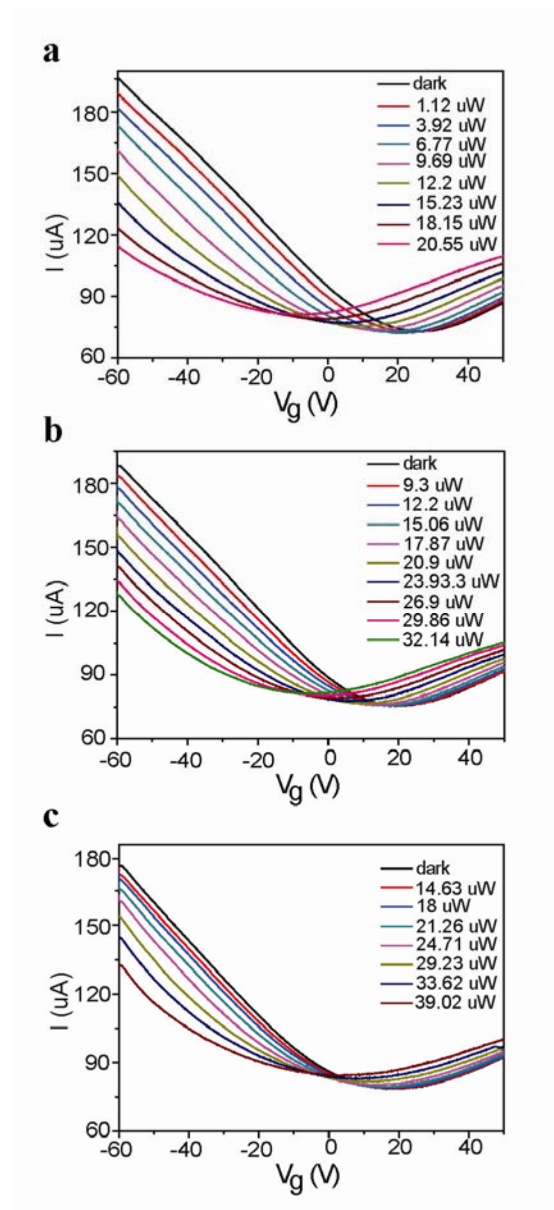

Figure S6 Near to mid-infrared photoresponse of the graphene/Si/graphene heterostructure photodetector. I-V_g characteristics of graphene photodetector under different illumination power with the excitation wavelength at **(a)** 1.3 µm, **(b)** 2.1 µm, and **(c)** 3.2 µm, respectively. V_{SD} = 1.5V.

© 2014 Macmillan Publishers Limited. All rights reserved.

Reference:

1 Kim, S. *et al.* Direct measurement of the Fermi energy in graphene using a double-layer heterostructure. *Phys. Rev. Lett.* **108,** 116404 (2012).
2 Lee, E. J. H., Balasubramanian, K., Weitz, R. T., Burghard, M. & Kern, K. Contact and edge effects in graphene devices. *Nature Nanotechnol.* **3,** 486-490 (2008).
3 Xu, X. D., Gabor, N. M., Alden, J. S., van der Zande, A. M. & McEuen, P. L. Photo-thermoelectric effect at a graphene interface junction. *Nano Lett.* **10,** 562-566 (2010).
4 Park, J., Ahn, Y. H. & Ruiz-Vargas, C. Imaging of photocurrent generation and collection in single-layer graphene. *Nano Lett.* **9,** 1742-1746 (2009).
5 Xia, F. N. *et al.* Photocurrent imaging and efficient photon detection in a graphene transistor. *Nano Lett.* **9,** 1039-1044 (2009).
6 Liu, C. H., Dissanayake, N. M., Lee, S., Lee, K. & Zhong, Z. H. Evidence for extraction of photoexcited hot carriers from graphene. *ACS Nano* **6,** 7172-7176 (2012).

© 2014 Macmillan Publishers Limited. All rights reserved.